

This manuscript “Considering fault interaction in estimates of solute stress along faults in the San Gorgonio Pass region, southern California” is a non-peer reviewed preprint, which has been submitted to Geosphere for peer review for the themed issue on the Seismotectonics of the San Andreas fault in the San Gorgonion Pass Region. We encourage your feedback.

Jennifer Hatch ([jbeyer@geo.umass.edu](mailto:jbeyer@geo.umass.edu)) corresponding author  
University of Massachusetts Amherst

Michele Cooke ([cooke@geo.umass.edu](mailto:cooke@geo.umass.edu))  
University of Massachusetts Amherst

Aviel Stern  
University of Massachusetts Amherst

Roby Douilly  
University of California Riverside

David Oglesby  
University of California Riverside

1 **Considering fault interaction in estimates of absolute stress along**  
2 **faults in the San Gorgonio Pass region, southern California**

3  
4 **Jennifer Hatch<sup>1</sup>, Michele L. Cooke<sup>1</sup>, Aviel Stern<sup>1</sup>, Roby Douilly<sup>2</sup>, David Oglesby<sup>2</sup>**

5 <sup>1</sup>*Department of Geosciences, University of Massachusetts, Amherst, MA 01003*

6 <sup>2</sup>*Department of Earth Sciences, University of California, Riverside, CA 92521*

7  
8 **ABSTRACT**

9 Present-day shear tractions along faults of the San Gorgonio Pass region can be estimated  
10 from stressing rates provided by three-dimensional forward crustal deformation models.  
11 Modeled dextral shear stressing rates on the San Andreas and San Jacinto faults differ from rates  
12 resolved from the regional loading due to fault interaction. In particular, fault patches with  
13 similar orientations and depths on the two faults show different stressing rates. We estimate the  
14 present-day, evolved fault tractions along faults of the San Gorgonio Pass region using the time  
15 since last earthquake, fault stressing rates (which account for fault interaction), and co-seismic  
16 models of the impact of recent nearby earthquakes. The evolved tractions differ significantly  
17 from the resolved regional tractions, with the largest dextral traction located within the  
18 restraining bend comprising the pass, which has not had recent earthquakes, rather than outside  
19 of the bend, which is more preferentially oriented under tectonic loading. Evolved fault tractions  
20 can provide more accurate initial conditions for dynamic rupture models within regions of  
21 complex fault geometry, such as the San Gorgonio Pass region. An analysis of the time needed to  
22 accumulate shear tractions that exceed typical earthquake stress drops shows that present-day  
23 tractions already exceed 3 MPa along portions of the Banning, Garnet Hill, and Mission Creek  
24 strands of the San Andreas fault. This result highlights areas that may be near failure if  
25 accumulated tractions equivalent to typical earthquake stress drops precipitate failure.

26



27 **Keywords:** San Andreas fault, San Gorgonio Pass, fault tractions, fault stressing rates, fault  
28 interaction, seismic hazard

29

## 30 **1. INTRODUCTION**

31 The southern San Andreas fault system consists of multiple active faults that  
32 accommodate the deformation between the North American and Pacific plates. Accurate  
33 estimates of the earthquake hazard in California require an accurate assessment of the potential  
34 for large through-going earthquakes and the ability for ruptures to propagate through fault  
35 intersections and complexities (e.g., Field et al., 2013). One region of such complexity is the San  
36 Gorgonio Pass region (SGPr), a restraining stepover along the southern San Andreas fault  
37 (Figure 1). Accurate dynamic rupture models of the SGPr that simulate potential rupture paths  
38 will help us assess the potential for large and damaging earthquakes through this region (e.g.,  
39 Tarnowski, 2017; Douilly et al., 2017).

40 Dynamic rupture models show that, in general, the size and extent of earthquake ruptures  
41 can depend highly on the initial conditions of the model (e.g., Oglesby et al., 2005). These  
42 conditions include physical aspects, such as fault geometry and location of rupture nucleation  
43 (e.g., Lozos et al., 2012; Lozos, 2016; Tarnowski, 2017), and time-dependent aspects, such as  
44 state of stress and frictional parameters (e.g., Kame et al., 2003; Aochi and Olsen, 2004; Kase  
45 and Day, 2006; Duan and Oglesby, 2007). Dynamic rupture models typically prescribe initial  
46 shear and normal tractions by resolving the remote stress tensor, constrained from focal  
47 mechanism inversions, onto individual fault elements (e.g., Kame et al., 2003; Oglesby et al.,  
48 2003). This approach provides spatially variable ‘resolved’ tractions that capture the first-order  
49 loading of the faults but does not take into account the loading history, nor the prior stress

50 interactions between faults. Not only can individual earthquake events change tractions along  
51 nearby faults, advancing or retarding each faults' earthquake clock (e.g., King et al., 1994; Stein,  
52 1999; Duan and Oglesby, 2005), but interaction among neighboring active faults influences their  
53 long-term slip rates and stressing rates (Willemse and Pollard, 1998; Maerten et al., 1999;  
54 Loveless and Meade, 2011). Stressing rates on any given fault can be estimated using geodesy  
55 (e.g., Smith and Sandwell, 2006). However, the total accumulated traction along any given fault  
56 segment depends on the accumulated tractions during the interseismic period as well as nearby  
57 rupture history (e.g., Smith-Konter and Sandwell, 2009; Richards-Dinger and Dieterich, 2012;  
58 Tong et al., 2014).

59         To account for loading history and fault interaction and produce more accurate estimates  
60 of fault stress, we simulate deformation within the San Gorgonio Pass region using three-  
61 dimensional forward models that provide both slip rates over multiple earthquake cycles and  
62 stressing rates between earthquake events. Because we use slip rates over multiple earthquake  
63 cycles to drive models that simulate interseismic deformation, the resulting shear stressing rates  
64 incorporate the interactions between faults of the southern San Andreas fault system. The  
65 interseismic shear stressing rates along with information about time since last earthquake event  
66 can be used to estimate the shear traction on faults through the SGPr following the approach  
67 employed by Tong et al. (2014). The resulting estimates of shear traction may differ from  
68 resolving the remote stress tensor onto faults in that our models explicitly include fault  
69 interaction and fault loading from depth during the interseismic period. Furthermore, we  
70 incorporate the effects of recent earthquakes on faults near the SGPr to produce a more accurate  
71 estimate of the current stress state of this system. Using tractions that incorporate fault  
72 interaction and loading history may enhance the accuracy of dynamic rupture models, refining

73 our insight into the nature of potential earthquake rupture propagation within the San Gorgonio  
74 Pass region.

75

## 76 **2. REGIONAL GEOLOGY – THE SAN GORGONIO PASS REGION**

77 Through the San Gorgonio Pass region (SGPr), deformation is partitioned onto multiple,  
78 active and nonvertical fault strands (e.g., Matti et al., 1992; Figure 1). The San Bernardino strand  
79 of the San Andreas fault lies at the northwest end of the San Gorgonio Pass. Two potential  
80 rupture pathways go through the restraining bend connecting the San Bernardino strand to the  
81 Coachella segment of the San Andreas fault. The southern pathway consists of the San Gorgonio  
82 Pass thrust, Garnet Hill strand, and Banning strand of the San Andreas fault (Figure 1). The San  
83 Gorgonio Pass thrust dips to the north and has a corrugated geometry near the Earth's surface  
84 (e.g., Matti et al., 1992). The eastern end of the San Gorgonio Pass thrust connects to the Garnet  
85 Hill and Banning strands. The north-dipping Garnet Hill and subparallel Banning strands have  
86 approximately the same strike. The northern pathway through the SGPr consists of the Mill  
87 Creek, Mission Creek, and Galena Peak strands of the San Andreas fault (Figure 1). Ongoing  
88 debate centers on the geometry and activity of these fault strands through the northern part of the  
89 SGPr (e.g., Kendrick et al., 2015; Beyer et al., 2018; Fosdick and Blisniuk, 2018). The San  
90 Jacinto fault is sub-parallel to the San Andreas fault and extends to within 2 km of the San  
91 Andreas fault at Cajon Pass. While the San Jacinto fault lies outside of the SGPr, it interacts with  
92 the San Andreas fault and consequently impacts both long-term slip rates (e.g., Herbert et al.,  
93 2014) and earthquake rupture paths (Lozos, 2016) on the San Andreas fault.

94 Recent paleoseismic data within the SGPr suggest that previous large through-going  
95 earthquakes have a recurrence interval of ~ 1000 years, with the most recent earthquake rupture

96 through the San Gorgonio Pass along the southern pathway in 1400 AD (Heermance and Yule,  
97 2017). Earthquakes along the San Bernardino strand (north of the restraining bend) and  
98 Coachella segment of the San Andreas fault (south of the bend) occur more frequently, with  
99 recurrence intervals of 200-300 years (e.g., Philibosian et al., 2011; Field et al., 2013; Onderdonk  
100 et al., 2018). The difference in recurrence intervals outside of and inside of the restraining bed  
101 suggests that previous earthquakes that have ruptured along the San Bernardino and Coachella  
102 segments terminated at the restraining bend, which may be acting as an ‘earthquake gate’.  
103 During the interseismic period since the last rupture event through the bend, shear tractions have  
104 been accumulating along faults within the SGPr. Furthermore, recent earthquakes along faults  
105 surrounding the SGPr could impact the state of stress within the San Gorgonio Pass, and thus the  
106 shear and normal tractions along the faults.

107

## 108 **2.1 Recent earthquakes near the San Gorgonio Pass region**

109 To calculate the stress interaction effects from past earthquakes, we consider records of three  
110 ground-rupturing earthquakes that occurred within the past 300 years near the SGPr. While many  
111 smaller earthquakes have occurred within this region, these larger ground-rupturing events have  
112 the greatest potential to impact tractions along nearby faults.

### 113 **2.1.1 1992 Landers Earthquake**

114 The Landers earthquake occurred on June 28, 1992, rupturing five fault segments,  
115 striking northwest-southeast, in the Eastern California Shear Zone (Hart et al., 1993). The  
116 interaction of these faults created a linked fault network that generated an M7.3 earthquake,  
117 which is larger than expected for any single fault involved in the rupture (Aydin and Du, 1995).  
118 The total rupture length is estimated at 85 km on the primary rupture trace (Sieh et al., 1993).

119 The epicenter was located on the south portion of the Johnson Valley Fault, and the rupture  
120 traveled northward along the Landers-Kickapoo, Homestead Valley, Emerson, and Camp Rock  
121 faults, crossing two extensional stepovers and one compressional stepover (e.g., Aydin and Du,  
122 1995; Madden and Pollard, 2012), while only rupturing parts of the Johnson Valley, Emerson,  
123 and Camp Rock faults (Sieh et al., 1993). All of the involved faults were previously mapped,  
124 with the exception of the Landers-Kickapoo fault (Hart et al., 1993). The Johnson Valley and  
125 Landers-Kickapoo faults each slipped locally more than 2 m and the central portion of the  
126 Homestead Valley fault slipped more than 3 m (Sieh et al., 1993; Aydin and Du, 1995). Slip  
127 exceeded 4 m on the Emerson fault, and a maximum dextral slip of approximately 6 meters  
128 occurred on the North Emerson Fault (Bryant, 1992; Sieh et al., 1993; Bryant, 1994).

129

### 130 **2.1.2 1812 Wrightwood Earthquake**

131 The ~M7.5 earthquake that occurred on December 8, 1812 (here referred to as the  
132 Wrightwood earthquake), is one of the earliest earthquakes documented in the historical records  
133 of California; the rupture origin and extent are still uncertain. Evidence of this event has been  
134 observed within several paleoseismic trench sites along the San Andreas fault north of Cajon  
135 Pass (Weldon and Sieh, 1985; Seitz et al., 1997; Biasi et al., 2002; Fumal et al., 2002; Weldon et  
136 al., 2002), with a maximum dextral slip of 4-6 m and possible northern rupture extent ~100 km  
137 north of the Cajon Pass (Bemis et al., 2016). The southern extent of rupture is not well  
138 constrained. The most recent event recorded at Plunge Creek on the San Bernardino strand (site 3  
139 Fig.1) is dated to within the 1600s (McGill et al., 2002), but minor slip on secondary structures  
140 farther south along the San Bernardino strand, near Burro Flats (site 4 Fig. 1), dates to the early  
141 1800s (Yule and Howland, 2001). Several paleoseismic sites along the northernmost strand of

142 the San Jacinto fault record 1.8-3 m of slip during an early 1800s earthquake event (Kendrick  
143 and Fumal, 2005; Onderdonk et al., 2013; Onderdonk et al., 2015). Several have suggested the  
144 plausibility of the 1812 earthquake jumping the < 2 km extensional stepover between the San  
145 Andreas and San Jacinto faults (Figure 1) and involving both faults (Onderdonk et al., 2013;  
146 Onderdonk et al., 2015; Rockwell et al., 2015). Lozos (2016) used dynamic rupture models to  
147 investigate rupture scenarios that best fit the paleoseismic evidence and historical accounts of the  
148 Wrightwood earthquake. The models of Lozos (2016) suggest that the Wrightwood earthquake  
149 nucleated near Mystic Lake on the San Jacinto fault (site 8 Fig. 1), produced a maximum of 6 m  
150 of slip near Colton, and propagated north onto the San Andreas fault (maximum of 4-5 m of slip  
151 between Cajon Pass and Wrightwood).

152

### 153 **2.1.3 1726 Coachella Valley Earthquake**

154 The Coachella segment of the southern San Andreas fault has not experienced a large  
155 earthquake in historical time. Paleoseismic studies reveal that the most recent earthquake is dated  
156 to  $1726 \pm 7$  (Rockwell et al., 2018), with a possible rupture trace extending from Salt Creek site  
157 along the Salton Sea (site 7 Fig. 1; Sieh and Williams, 1990) to the Thousand Palms oasis site on  
158 the Mission Creek strand (site 5 Fig. 1; Fumal et al., 2002), with at least 2 m of dextral offset at  
159 the Indio site on the Coachella segment (site 6 Fig. 1; Sieh, 1986).

160

## 161 **3. METHODS**

162 We use Poly3D, a quasi-static, three-dimensional boundary element method code, to  
163 simulate loading and interseismic deformation along the southern San Andreas fault system.  
164 Poly3D solves the relevant equations of continuum mechanics to calculate stresses and

165 displacements throughout the model (e.g., Thomas, 1993; Crider and Pollard, 1998). Faults are  
166 discretized into triangular elements of constant slip (no opening/closing is permitted) within a  
167 linear-elastic half-space. The element size along the faults of the San Gorgonio Pass region  
168 (SGPr) average ~4 km and allow for our models to capture fault irregularities as small as ~10  
169 km. We simulate the active fault geometry of the southern San Andreas fault, the San Jacinto  
170 fault, and the Eastern California Shear Zone (Figure 2) based on the Southern California  
171 Earthquake Center's Community Fault Model (CFM) version 4.0 (Plesch et al., 2007; Nicholson  
172 et al., 2017). The CFM is compiled from geologic mapping, seismicity, and geophysical data.  
173 While the CFM has been updated to version 5.2, the interpreted active fault geometry of the San  
174 Gorgonio Pass region is still under debate (e.g., Kendrick et al., 2015; Beyer et al., 2018; Fosdick  
175 and Blisniuk, 2018). We use version 4.0 of the CFM but include fault geometry modifications  
176 that serve both to improve the representation of the mapped active fault geometry and to improve  
177 the match of model and geologic uplift patterns and slip rates in the San Gorgonio Pass region  
178 (e.g., Cooke and Dair, 2011; Herbert and Cooke, 2012; Fattaruso et al., 2014; Beyer et al., 2018).

179       Faults in the CFM are defined to the base of the seismogenic crust. To simulate long-term  
180 and interseismic deformation, we extend the faults down to a freely slipping, horizontal basal  
181 crack at 35 km depth that simulates distributed deformation below the seismogenic zone  
182 (Marshall et al., 2009). This modification eliminates artifacts that develop when the long-term  
183 slip rates go to zero at the base of the CFM-defined faults (Figure 2). Across many earthquake  
184 cycles, deformation patterns are primarily controlled by fault geometry (e.g., Dawers and  
185 Anders, 1995; Fay and Humphreys, 2005; Herbert and Cooke, 2012). Therefore, to capture the  
186 first-order loading of active faults, we do not consider potential secondary impacts of  
187 heterogeneous and/or anisotropic rock properties.

188           We prescribe the tectonic loading on the boundaries of the model base, far from  
189 investigated faults. Following Beyer et al. (2018), we implement an iterative technique that  
190 ensures a uniform tectonic velocity, determined from geodetic estimates (DeMets and Dixon,  
191 1999) at the model edges that are sub-parallel to the plate boundary (sides labeled I on Figure 2)  
192 and a linear velocity gradient at the models edges that cross the plate boundary (sides labeled II  
193 on Figure 2). The iterative approach of Beyer et al. (2018) ensures that applied velocities are  
194 within ~1% of the desired tectonic loading. For faults that extend beyond our model area (San  
195 Andreas, San Jacinto, and Cucamonga-Sierra Madre fault systems), we apply slip rates to distal  
196 edge patches of these faults to prevent non-zero slip rates on these faults at the edge of our  
197 model. We apply 35 mm/yr dextral slip to the San Andreas fault at the northwestern edge of the  
198 model (Weldon and Sieh, 1985). At the southeastern edge, we prescribe 25 mm/yr dextral slip to  
199 the San Andreas fault and 10 mm/yr dextral slip to the San Jacinto fault (e.g., Sharp, 1981;  
200 Becker et al., 2005; Fay and Humphreys, 2005; Meade and Hager, 2005). Because of complex  
201 fault geometry and interaction among faults, deformation within the SGPr is not impacted  
202 significantly by variations in the partitioning of slip rates between the San Andreas and San  
203 Jacinto faults at this model edge (Fattaruso et al., 2014). We apply 1.6 mm/yr reverse slip  
204 (McPhillips and Scharer, 2018) to the western edge of the modeled Cucamonga fault to account  
205 for deformation along the Sierra Madre fault not included in our model.

206           We use a two-step modeling approach to estimate the interseismic stressing rates along  
207 the southern San Andreas fault system. The first model simulates deformation over many  
208 earthquake cycles (steady state model) providing slip-rate information to a second model  
209 (interseismic model) that simulates the build-up of stress between earthquakes due to constant  
210 slip below the locking depth. In the steady state model, tectonic loading is prescribed along the



211 model edges at the base of the model, far from the investigated faults. The faults throughout the  
212 model have zero shear traction and slip freely in response to tectonic loading and fault  
213 interaction. This zero-shear traction simulates the low dynamic strength of faults during rupture  
214 (e.g., Di Toro et al., 2006; Goldsby and Tullis, 2011). We simulate interseismic deformation by  
215 applying the distribution of slip rates determined with the steady state model to fault surfaces  
216 below the prescribed locking depth and lock fault elements above the locking depth. The abrupt  
217 transition from locked to slipping at the specified locking depth used here produces stresses that  
218 are unreliable within one element of the transition, or  $\sim 5$  km. We use a locking depth of 25 km  
219 to ensure that our model results provide reliable fault tractions to about 20 km depth that can be  
220 used within dynamic rupture simulations within the full depth of the seismogenic crust.

221

### 222 **3.1 Estimating the impact from nearby recent earthquakes**

223 We simulate the 1992 Landers earthquake, 1812 Wrightwood earthquake, and 1726  
224 Coachella Valley earthquakes by prescribing the interpreted co-seismic slip distribution  
225 associated with each earthquake (e.g., Sieh, 1986; Hart et al., 1993; Onderdonk et al., 2015) to  
226 the modeled fault surfaces. We segment the rupture surface into multiple vertical segments and  
227 prescribe each segment a uniform slip according to the observations at the rupture trace (Figure  
228 4). All other faults in the model are locked, and we do not consider the effect of tectonic loading  
229 while simulating each earthquake due to the short rupture time. The resulting static stress  
230 changes due to each earthquake alters tractions along the faults within the SGPr.

231

### 232 **3.2 Estimating evolved tractions**

233 The interseismic model determines stressing rates due to deep movement below the

234 seismogenic crust and uses these stressing rates to calculate current shear tractions along the fault  
235 segments of the southern San Andreas fault within the SGPr using the time since the last rupture.  
236 Estimating both shear and normal tractions from stressing rates requires an assumption on how  
237 such accumulated tractions may dissipate with time. This approach relies on the premise that  
238 shear tractions that accumulate during the interseismic period are released during earthquake  
239 events. Because normal tractions that accumulate in the interseismic period, such as within  
240 restraining bends, are not necessarily relieved upon fault slip, models of earthquake cycles  
241 require dissipation mechanisms in order to avoid singular-valued normal tractions. Duan and  
242 Oglesby (2006) simulate multiple earthquake cycles by coupling a viscoelastic interseismic  
243 model with an elastic dynamic rupture model, such that normal stresses are relaxed during the  
244 interseismic period in the viscoelastic model and used as input to the dynamic rupture model.  
245 Alternatively, the Rate and State Earthquake Simulator (RSQSIM) employs a constant, but  
246 spatially variable normal stress distribution and disregards accumulated normal tractions (e.g.,  
247 Richards-Dinger and Dieterich, 2012). Here, we follow the approach of RSQSIM and do not  
248 carry the normal stressing rates through the rest of the analysis.

249       To estimate the shear traction that evolves over the earthquake cycle, henceforth called  
250 the evolved shear traction, we follow Tong et al. (2014) and use the stressing rate information  
251 from the interseismic model and the time since last event for each fault. In this approach, we  
252 only consider large ground-rupturing events that are preserved in the paleoseismic record. The  
253 approach analyzes a coseismic stress drop corresponding to the change from static friction to  
254 dynamic friction during large ground-rupturing earthquakes (shaded region in Figure 3). If the  
255 dynamic strength of the fault is near zero, a complete stress drop is associated with these events.  
256 Such complete stress drop is consistent with recent field measurements of low temperatures

257 along recently ruptured fault surfaces, a result of a very low dynamic friction (e.g., Carpenter et  
258 al., 2012, Fulton et al., 2013, Li et al., 2015), as well as high-speed laboratory frictional  
259 experiments cited above. Consequently, the associated shear traction at any time in the  
260 earthquake cycle is

$$261 \quad \tau = \dot{\tau} \cdot t \quad (1)$$

262 where  $\tau$  is the evolved shear traction,  $\dot{\tau}$  is the shear stressing rate and  $t$  is the time since last  
263 event. We sum the evolved shear tractions calculated by Equation 1 and the static stress changes  
264 due to nearby earthquakes to produce the present-day evolved shear tractions along the faults  
265 within the SGPr. This simplified approach to estimate the distribution of present-day shear  
266 tractions may provide more accurate initial conditions than the approach employed by dynamic  
267 rupture models of estimating tractions by resolving the remote loading onto the faults because  
268 the evolved tractions also incorporates both loading history and fault interaction, by including  
269 long term slip rates at depth and recent nearby earthquake events (Figure 3).

270

### 271 **3.3 Consideration of geometric and tectonic uncertainty**

272 Using models of deformation over multiple earthquake cycles, Beyer et al. (2018)  
273 compared the slip rate distribution from six plausible active fault configuration models to  
274 available geologic slip rate data. The analysis revealed that two active fault configurations  
275 provide the best fit to the geologic observations. For this study, we use both of the two best-fit  
276 models: the *Inactive Mill Creek* and *West Mill Creek* models from Beyer et al. (2018). The most  
277 pronounced fault geometry difference between the two configurations is the addition of a  
278 through-going Mission/Mill Creek strand through the northern part of the SGPr in the *West Mill*  
279 *Creek* model. Here, we present the results of the *Inactive Mill Creek* model geometry, and the

280 Supplemental Material contains the results of the *West Mill Creek* model geometry. Following  
281 Herbert and Cooke (2012), Beyer et al. (2018) also tested each of the plausible fault  
282 configurations under a range of reasonable tectonic loading (45-50 mm/yr at 340°-345°; DeMets  
283 and Dixon, 1999); for this study, we use the mean slip rate from the end members of permissible  
284 tectonic loadings.

285

## 286 **4. RESULTS**

287 We present the interseismic stressing rates for faults of the San Gorgonio Pass region  
288 (SGPr) and show the impact of fault interaction on these rates. We analyze the results of the  
289 models that simulate three recent ground-rupturing earthquakes and the impact of these  
290 earthquakes on fault tractions within the SGPr. We then calculate the total evolved shear  
291 tractions that incorporate the impacts of both fault interaction and loading history.

292

### 293 **4.1 Stressing rates**

294 Maps of interseismic shear stressing rate along the southern San Andreas fault reveal how  
295 the fault geometry controls the stressing rate distribution (Figure 5). Figure 5 shows stressing  
296 rates for the *Inactive Mill Creek* model configuration (Figure 5A and 5C) and the difference in  
297 stressing rates between the two plausible active fault geometries (Figure 5B and 5D). Dextral  
298 shear stressing rates are larger (maximum 12 kPa/yr) than the reverse-shear stressing rates  
299 (maximum ~3 kPa/yr) along the San Andreas fault. Furthermore, portions of the faults parallel to  
300 the overall plate motion, outside of the restraining bend, have greater dextral stressing rate than  
301 faults within the bend. Dextral shear stressing rates are largest along the San Bernardino and  
302 Mission Creek strands of the SAF and decrease within the restraining bend of the SGPr (Figure

303 5A). The San Gorgonio Pass thrust has an undulating strike and small sinistral shear stressing  
304 rates occur locally along patches of the western San Gorgonio Pass thrust where the strike is less  
305 than  $\sim 265^\circ$ . The reverse-shear stressing rates are near zero outside the restraining bend and  
306 increase within the bend along north-dipping fault strands that strike obliquely to the plate  
307 motion and accommodate uplift (Figure 5C). Stressing rates increase with depth, consistent with  
308 the deep slip that is applied to faults in the interseismic model. The difference in stressing rates  
309 between the two best-fitting model geometries (Figure 5B and 5D) are lower than 1 kPa/yr and  
310 indicate that the *West Mill Creek* fault geometry produces higher dextral stressing rates (blue)  
311 throughout most of the region. The greatest difference in reverse-shear stressing rates is limited  
312 to within and just outside the bend. We only consider the *Inactive Mill Creek* fault geometry for  
313 the rest of our analysis, and consequently, reported shear tractions may underestimate by  $\sim 2\%$   
314 shear tractions if the true active fault geometry is closer to the configuration of our *West Mill*  
315 *Creek* model.

316 To the first order, the strike-parallel shear stressing rate along the southern San Andreas  
317 fault correlates with the orientation of the fault segments relative to the applied model loading  
318 that simulates plate motions. Previous models of the region have shown significant interaction  
319 between the San Andreas and San Jacinto faults (Herbert et al., 2014; Fattaruso et al, 2014), so  
320 we expand the analysis of stressing rates to include both of these faults in order to investigate the  
321 influence of fault interaction on stressing rates. The model produces different interseismic  
322 dextral shear stressing rates along similarly oriented portions of the San Andreas and San Jacinto  
323 faults. Figure 6 shows a gridded surface fit through model data points (white circles) of dextral  
324 stressing rates for different strikes and depths of the San Andreas (Figure 6A) and San Jacinto  
325 faults (Figure 6B). Stressing rates for both faults increase with depth, and in general, dextral

326 stressing rates are higher on the San Andreas fault than on the San Jacinto fault for locations with  
327 the same strike and depth. For the San Andreas fault, maximum dextral stressing rate occurs at  
328 strikes between  $300^{\circ}$ - $305^{\circ}$ . Relative to the San Andreas, the variation of dextral stressing rate  
329 with strike along the San Jacinto fault is more subdued, but the distribution shows a maximum  
330 strike stressing rate along segments that strike  $\sim 310^{\circ}$ . Both of these maximum shear orientations  
331 differ from the orientation expected from resolving the regional stress tensor (black line in Figure  
332 6). The difference between dextral stressing rates along the San Andreas and San Jacinto faults  
333 and the expected distribution from resolved tractions demonstrates the strong impact of fault  
334 interaction on the distribution of fault stressing rates.

335         The impact of fault interaction is also demonstrated in the relative stressing rates on the  
336 Banning and Mission Creek strands, which differs between the two plausible fault configurations  
337 (Figure 5). The presence of a through-going Mission Creek fault in the *West Mill Creek* model  
338 geometry (Figure S1) shifts strike-parallel shear stressing rates from the Banning strand to the  
339 Mission Creek strand by  $\sim 0.1$  kPa/yr. These differences in stress accumulation rates over the  
340 interseismic period demonstrates that fault interaction impacts the distribution of accumulated  
341 tractions along faults within a complex system.

342

#### 343 **4.2 Impact of stresses from regional earthquakes**

344         To assess the impact of the recent nearby earthquakes along faults within the SGPr, we  
345 numerically simulate three ground-rupturing earthquakes. We simulate the Landers Earthquake,  
346 Wrightwood Earthquake, and Coachella Valley Earthquake and examine the static stress change  
347 due to each event (Figure 7). Because we do not consider the potential relaxation of these crustal  
348 stresses over time (e.g., Pollitz and Sacks, 2002), the fault tractions from earthquakes modeled

349 provide an upper bound to expected tractions.

350         The modeled static stress change from the 1992 Landers earthquake impacts tractions  
351 along faults within the San Gorgonio Pass restraining bend. The change in dextral tractions  
352 (positive) reach a maximum of  $\sim 0.1$  MPa, along the San Gorgonio Pass thrust and a change in  
353 sinistral tractions (negative) of up to 0.15 MPa on the southern Garnet Hill, Banning, and  
354 Mission Creek strands of the SAF (Figure 7A). The San Gorgonio Pass region lies in the  
355 extensional quadrant of the Landers rupture, and as a result, the fault strands within the bend are  
356 loaded with normal dip-slip tractions of  $\sim 0.13$  MPa. This dip-slip traction change effectively  
357 reduces the accumulated long-term reverse dip-slip traction on these faults.

358         Change in co-seismic dextral tractions due to the 1812 Wrightwood earthquake increase  
359 the most (1.3 MPa) just south of the rupture limit on the San Bernardino strand, while the  
360 southernmost portion of the San Bernardino strand experiences sinistral traction changes of  $\sim$   
361 0.25 MPa (Figure 7B). The western San Gorgonio Pass thrust is loaded with dextral tractions ( $\sim$   
362 0.4 MPa), while the Garnet Hill, Banning and Mission Creek strands experience slight ( $< 0.1$   
363 MPa) increases in sinistral shear tractions. Furthermore, the western-most extent of the San  
364 Gorgonio Pass thrust has normal dip-slip shear, while the rest of the thrust and Garnet Hill strand  
365 has reverse dip-slip shear. These complex fault stressing patterns result from the location and  
366 orientation of the faults in relation to the Wrightwood rupture path. The close proximity of the  
367 dextral slip on the SJF to the subparallel fault strands of the SAF results in sinistral co-seismic  
368 traction changes on the SAF, which sits in the stress shadow of the Wrightwood earthquake.

369         Traction changes imposed on the San Gorgonio Pass fault strands due to the 1726  
370 Coachella Valley earthquake reach  $\sim 1$  MPa on the Mission Creek ahead of the rupture  
371 termination and  $\sim 0.8$  on the Banning strands near the junction with the Coachella segment

372 (Figure 7C). Dextral tractions of up to ~ 0.1 MPa extend into the restraining bend. While these  
 373 nearby earthquakes are shown here to impact the SGPr, all the resulting static stress changes due  
 374 to these earthquakes are small compared to the total tractions accumulated along these faults  
 375 during the interseismic period.

376

### 377 **4.3 Estimate evolved stresses**

378 Paleoseismic data provide estimates for the time since last event,  $t$ , along active faults  
 379 (e.g., Biasi et al., 2009; Table 1). We estimate the total present-day traction along each fault  
 380 segment by summing the tractions from Equation 1 with the static traction change of each nearby  
 381 earthquake. For the San Bernardino segment, we use time since last event from the compiled  
 382 earthquake data of Biasi et al. (2009). Paleoseismic sites at Pitman Canyon (site 2 Fig. 1), Plunge  
 383 Creek (site 3 Fig. 1), and Wrightwood (site 1 Fig. 1) provide a mean  $t$  of 207 years for the San  
 384 Bernardino segment. Paleoseismic constraints from the Thousand Palms Oasis site (site 5 Fig. 1;  
 385 Fumal et al., 2002) is used for the Mission Creek strand and the Coachella site (site 6 Fig. 1;  
 386 Philibosian et al., 2011) for the Coachella segment. These studies are in agreement that the last  
 387 rupture event occurred circa 1680. This event has been re-dated by Rockwell et al. (2018) to be  
 388 around the year  $1726 \pm 7$ . For the San Gorgonio Pass thrust, Banning, and Garnet Hill strands of  
 389 the SAF, we use an earthquake rupture year of 1400 (Heermance et al., 2017; Yule et al., 2014).

390

Fault strand(s)	Paleoseismic Site(s)	Most recent EQ Year (AD)	Time since last event (yr)
San Bernardino	Pitman Canyon/Plunge Creek/Wrightwood ( <i>Biasi et al., 2009</i> )	1812	207
Banning/SGPT/Garnet Hill	Millard Canyon ( <i>Heermance et al., 2017, Yule et al., 2014</i> )	1400	619
Mission Creek/Coachella	1000 Palms/Coachella ( <i>Fumal et al., 2002; Philibosian et al., 2011;</i>	1726	293



	<i>Rockwell et al., 2018)</i>		
--	-------------------------------	--	--

391 Table 1: Time since last event data used to calculate absolute shear stress from the  
392 interseismic stressing rate.  
393

394       Due to the variable time since last earthquake event across faults of the SGPr, the evolved  
395 shear traction distribution along the fault surfaces (Figure 8A) differs significantly from the shear  
396 stressing rate distributions (Figure 5). Whereas dextral-shear stressing rates are lower along the  
397 north-dipping fault surfaces within the SGPr restraining bend than on fault surfaces outside of  
398 the bend (Figure 5A), the longer  $t$  for the faults within the restraining bend increases the total  
399 accumulated dextral shear traction within the bend relative to other faults (Figure 8A). Similarly,  
400 although the Coachella segment and the San Bernardino strand of the SAF have greater dextral  
401 stressing rates than the restraining segment, the more recent rupture of these segments in the  
402 1726 and 1812 events, respectively, reduces the accumulated tractions outside the bend. The  
403 largest evolved dextral shear tractions arise along the Banning and Garnet Hill strands of the  
404 SAF near the juncture with the Coachella segment of the SAF (Figure 8A). Regions of high  
405 dextral shear traction also arise along portions of the San Gorgonio Pass thrust. The evolved  
406 reverse shear tractions are greatest along the San Gorgonio Pass thrust within the restraining  
407 bend. We note that if the true active fault geometry is closer approximated by the alternative  
408 fault configuration (Figure S1), the total evolved shear tractions may be underestimated by up to  
409 2%.

410       These evolved shear tractions take into account fault interaction (Figure 6), the  $t$  for each  
411 fault strand (Table 1), and the impact of recent nearby earthquakes (Figure 7). To assess the  
412 impact of fault history and interaction, we compare the evolved dextral shear traction (Figure  
413 8A) to the fault tractions that result from resolving the regional stress tensor constrained from  
414 focal mechanism inversions onto the faults (Figure 8B). Following Tarnowski (2017), we use the

415 orientation of the stress field and relative magnitude of the principal stress axes from Hardebeck  
416 and Hauksson (2001) and the stress ratio,  $A\phi$  (Simpson, 1997), of 1.5, which indicates a mixed  
417 strike-slip and thrust stress regime. The resulting stress tensor is scaled such that the change from  
418 static to dynamic friction results in a 3 MPa stress drop (e.g., Tarnowski, 2017) in order to  
419 represent the fault loading conditions preceding a large earthquake rupture. The larger magnitude  
420 of the resolved dextral shear tractions compared to the evolved tractions is due to the scaling of  
421 the regional stress to produce failure and a 3 MPa stress drop with a dynamic friction of 0.1. The  
422 evolved tractions to the current year (2019) are not explicitly at failure and these tractions  
423 exclude those required for dynamic sliding (non-shaded region of Figure 3). Consequently, we  
424 focus our comparison on the patterns of the evolved and resolved stresses rather than the  
425 absolute level of stress. The resolved tractions have greater lateral heterogeneity as the tractions  
426 range from 10 MPa dextral to -5 MPa sinistral shear traction, where portions of the San  
427 Gorgonio Pass thrust receives sinistral shear from resolved loading. In contrast, the evolved  
428 tractions show dextral shear tractions everywhere on faults of the SGPr. Whereas the evolved  
429 shear tractions increase with depth, the remote stress tensor is not resolved for different depths.

430

## 431 **5. DISCUSSION**

432 Here we discuss the impact of including fault interaction and the effects of recent nearby  
433 earthquakes on fault tractions, and the implications of this study's findings for seismic hazard  
434 assessment.

435

### 436 **5.1 Resolved tractions likely oversimplify initial conditions for rupture**

437 Rupture propagation within dynamic models highly depends on the initial conditions

438 used for the model (e.g., Kame et al., 2003; Duan and Oglesby, 2007; Lozos et al., 2012). These  
439 models have the power to simulate potential rupture size and extent, as well as potential rupture  
440 paths (e.g., Oglesby et al., 2003). Most rupture dynamic studies either use a homogeneous  
441 regional stress field (e.g., Lozos et al., 2012) or a regional stress field with spatially rotating  
442 principal stress (e.g., Aochi and Fukuyama, 2002) to estimate the initial shear tractions on fault  
443 segments. Resolving the regional stress tensor onto faults does not account for fault interaction  
444 or the rupture history of each fault. Whereas these effects may be minimal in regions with planar  
445 faults, we show here that within regions of fault complexity, fault interaction and loading history  
446 can advance, or retard, the fault towards failure. Prescribing tractions that incorporate the effects  
447 of fault interaction and the loading history of each fault may improve the accuracy of dynamic  
448 rupture models.

449         Due to fault interactions over multiple earthquake cycles and the variable time since last  
450 earthquake event across faults of the SGPr, the evolved shear traction distribution along the fault  
451 surfaces (Figure 8A) differs from the tractions resolved from the regional stress state (Figure  
452 8B). Whereas resolved dextral-shear tractions are lower along the north-dipping fault surfaces  
453 within the SGPr restraining bend than on faults outside of the bend (also seen in the stressing  
454 rates in Figure 5), the longer  $t$  for the faults within the restraining bend increases the total dextral  
455 shear traction compared to other faults (Figure 8A). Similarly, the more recent ruptures of the  
456 1726 and 1812 earthquake events reduce the accumulated tractions outside the bend, but not  
457 within. The largest dextral shear tractions arise along the Banning and Garnet Hill strands of the  
458 SAF, especially near the juncture of the Banning strand with the Coachella segment of the SAF  
459 (Figure 8A). Furthermore, the evolved stresses do not produce enigmatic left-lateral loading on  
460 portions of the San Gorgonio Pass thrust of the resolved stresses. These structures do not show

461 surface evidence for left-lateral slip (Yule and Sieh, 2003). Consequently, the pattern of  
462 consistent dextral shear traction produced by the evolved stresses that include fault interaction  
463 and interseismic loading agrees with geologic evidence. Including evolved stress state for initial  
464 conditions within dynamic rupture models can produce more accurate assessment of rupture  
465 behavior along complex fault systems.

466

## 467 **5.2 Implications for seismic hazard**

468 To assess how close the faults of the San Gorgonio Pass region (SGPr) are to failure  
469 within our model of evolved fault tractions, we analyze the time until failure for each fault  
470 element. To consider this, we calculate how many years are required from the present day to  
471 accumulate evolved net shear tractions equivalent to typical earthquake stress drops of 3 MPa  
472 (Figure 9A) and 10 MPa (Figure 9B) (e.g., Allman and Shearer, 2009; Goebel et al., 2015).  
473 Using this criterion, fault elements on the easternmost Banning, Garnet Hill, and Mission Creek  
474 strands currently exceed 3 MPa at the base of the model (ellipse in Figure 9A). When using 10  
475 MPa for the accumulated traction required to trigger the next earthquake, the first fault element  
476 to fail is on the San Bernardino strand at 584 years from now (ellipse in Figure 9B). The  
477 difference in vulnerable position within the fault system owes to the greater stressing rate along  
478 the San Bernardino strand compared to the other faults.

479 The time since last ground rupturing earthquake event for fault strands within and just  
480 outside the restraining bend are near or greater than the estimated recurrence interval for these  
481 fault strands, and paleoseismic studies in this region suggest these faults are probably overdue, or  
482 close to failure (Philibosian et al., 2011; Rockwell et al., 2018; Onderdonk et al., 2018).  
483 Consequently, while 3 MPa represents a low stress drop in the SGPr (Goebel et al., 2015), this

484 lower stress drop implies that these faults are close to failure, which is consistent with earthquake  
485 clock and recurrence intervals of these faults.

486

## 487 **6. CONCLUSIONS**

488 We use three-dimensional crustal deformation models to estimate present-day fault  
489 tractions in the San Gorgonio Pass region. The models that estimate interseismic stressing rates  
490 are loaded with deep slip rates determined from a multiple-earthquake-cycle model that  
491 explicitly includes fault interaction. Consequently, the interseismic stresses incorporate both  
492 regional tectonic loading and fault interaction. A gradient of increasing shear stressing rates with  
493 depth emerges from our models that is consistent with deep interseismic deformation. To  
494 investigate the role of fault interaction within our models, we compare our modeled dextral shear  
495 stressing rates for the San Andreas and San Jacinto faults, which have similar orientation.  
496 Subsequently, the interseismic stressing rates would be similar on the two faults if based solely  
497 on orientation with respect to remote loading. Significant differences in the patterns of stressing  
498 rates along patches of the San Andreas and San Jacinto faults with similar orientation and depth  
499 arise due to the interaction between these two faults.

500 The total evolved present-day shear tractions along the fault include both the accumulated  
501 stressing rates since the last earthquake event and the impact of nearby earthquakes. We simulate  
502 recent nearby ground-rupturing earthquakes with co-seismic models to investigate the impact of  
503 these rupture events on the stress state along the San Andreas fault within the San Gorgonio Pass  
504 region. The pattern of total evolved fault tractions differs from that of the interseismic stressing  
505 rates. Tractions are higher within the restraining bend than outside the bend because of the longer  
506 time since last event on these faults. Fault strands within the restraining bend have been loading

507 for twice as long as the Coachella segment to the south and three times as long as the San  
508 Bernardino strand to the north. Comparison of our evolved tractions to the tractions resolved  
509 from the local stress field shows distinct differences. While the linear gradient with depth  
510 emerges from our models, the resolved tractions are not depth dependent, and the gradient must  
511 be added. Because the evolved tractions account for loading history, the largest tractions occur  
512 within the restraining bend, which has the longer time since last event.

513 We investigate the time needed for the accumulated net shear traction on each fault  
514 element to exceed 3 MPa and 10 MPa, typical coseismic stress drop values. Because the  
515 interseismic stress rates differ for faults throughout the San Gorgonio Pass region, the location  
516 and timing of potential failure depends on the stress drop value used as the shear traction  
517 threshold. Assuming a lower stress drop value shows that faults in the San Gorgonio Pass are  
518 currently at failure, whereas higher stress drop values do not.

519 This approach provides a more heterogeneous, more accurate representation of the  
520 current stress state along the southern San Andreas fault than a simple regional stress tensor. In  
521 regions of complex fault geometry such as the San Gorgonio Pass region, an ‘earthquake gate’,  
522 the potential for a through-going rupture is unclear and stress state may have a large control on  
523 rupture behavior. Our evolved fault tractions can provide more realistic initial conditions for  
524 dynamic rupture models of these regions, and therefore improve seismic hazard assessments.

525

## 526 **ACKNOWLEDGEMENTS**

527 The project was funded by USGS External Research Program grant G15AP00068, NSF grant  
528 EAR 1623637, and the Southern California Earthquake Center (Contribution No. 9076). SCEC is  
529 funded by NSF cooperative agreement EAR-1600087 and USGS cooperative agreement  
530 G17AC00047.

531

532

## 533 **FIGURE CAPTIONS**

534 **Figure 1.** Map of the San Gorgonio Pass region (SGPr). While there has not been a rupture event  
535 in the SGPr since ~1400 AD, recent nearby earthquakes may impact the stress within the bend.  
536 Fault traces of the San Andreas fault are labeled (GP – Galena Peak, SGPT – San Gorgonio Pass  
537 Thrust). Rupture traces considered in this study are highlighted: Landers earthquake (dark red),  
538 Wrightwood earthquake (red), Coachella Valley earthquake (orange), and 1400 event (yellow).  
539 Paleoseismic sites are numbered as such: 1 – Wrightwood, 2 – Pitman Canyon, 3 – Plunge  
540 Creek, 4 – Burro Flat, 5 – Thousand Palms, 6 – Indio, 7 – Salt Creek, 8 – Colton, and 9 – Mystic  
541 Lake.

542  
543 **Figure 2.** Northward oblique view of the model setup. Tectonic loading is prescribed at the  
544 boundaries of the model base, such that sides labeled (I) have a uniform tectonic velocity parallel  
545 to the plate boundary and sides labeled (II) are prescribed a linear gradient in the tectonic loading  
546 across the plate boundary. The shear traction-free faults slip freely in response to the loading and  
547 fault interaction. Black box outlines the San Gorgonio Pass region. SAF - San Andreas fault; SJF  
548 - San Jacinto fault.

549  
550 **Figure 3.** Schematic sketch of fault loading through time. During the interseismic period, the  
551 earthquake clock of a fault can be advanced or retarded by earthquakes on other nearby faults. If  
552 the dynamic strength of the fault is near zero, then the stress drop associated with the change  
553 from static to dynamic friction is a complete stress drop.

554  
555 **Figure 4.** Northward oblique view of the San Gorgonio Pass region showing the distribution of  
556 the applied slip (in meters) associated with the nearby 1992 Landers (dark red), 1812  
557 Wrightwood (red), and 1726 Coachella Valley (orange) earthquakes.

558  
559 **Figure 5.** Modeled interseismic stressing rates along faults within the San Gorgonio Pass. This  
560 region is primarily loaded in dextral shear (red in A). North-dipping faults are also loaded in  
561 reverse dip slip (red in C). B and D show the difference in stressing rates between the two  
562 plausible fault configurations of Beyer et al. (2018); difference is slip rate from *Inactive Mill*  
563 *Creek* minus slip rate from *West Mill Creek* model configuration.

564  
565 **Figure 6.** Modeled dextral stressing rates plotted with depth and fault strike for the A) San  
566 Andreas fault and B) San Jacinto fault. Model results are plotted as white circles, and a best-fit  
567 surface is fitted through the data (background grid). Patches along the two faults with similar  
568 orientation and depth have different values of shear stressing rates due to fault interaction. The  
569 orientations of magnitude of dextral shear stressing rate for both faults differ from the maximum  
570 shear direction predicted from the regional stress tensor (vertical black lines).

571  
572 **Figure 7.** Static stress changes from modeled recent, nearby earthquakes resolved as right-lateral  
573 tractions along faults of the SGPr. The Landers earthquake (A) increased dextral shear tractions  
574 along the San Bernardino strand and San Gorgonio Pass thrust, and decreased dextral shear  
575 tractions along the Garnet Hill, Banning, and Mission Creek strands. The Wrightwood  
576 earthquake (B) produces a complex change in tractions. The earthquake increased dextral shear  
577 tractions just east of the rupture termination on the San Bernardino strand but decreased dextral  
578 shear tractions further east due to the interaction with the neighboring San Jacinto fault, which  
579 had dextral slip. The Coachella Valley earthquake (C) increased dextral shear tractions on the

580 easternmost Mission Creek and Banning strands.

581  
582 **Figure 8.** Evolved (A) and Resolved (B) right-lateral tractions along faults of the SGPr. The  
583 increasing shear traction with depth emerges from the evolved stresses due to deep slip in  
584 the interseismic models. The resolved tractions show greater lateral variation than the evolved  
585 tractions. Arrows indicate the direction of principle compression.

586  
587 **Figure 9.** Faults of the SGPr colored by years until failure. (A) shows time until net shear  
588 tractions since the last earthquake exceed 3 MPa. With this criterion, fault elements on the  
589 Banning, Garnet Hill, and Mission Creek strands are currently at failure. (B) shows time until net  
590 shear tractions since the last earthquake exceed 10 MPa. Under this assumption, the first fault  
591 element to fail is on the San Bernardino strand at 584 years from present. Ellipses highlight the  
592 first elements to fail.

593  
594

## 595 REFERENCES

- 596 Allmann, B.P. and Shearer, P.M., 2009. Global variations of stress drop for moderate to large  
597 earthquakes. *Journal of Geophysical Research: Solid Earth*, 114(B1).
- 598 Aochi, H. and Fukuyama, E., 2002. Three-dimensional nonplanar simulation of the 1992 Landers  
599 earthquake. *Journal of Geophysical Research: Solid Earth*, 107(B2), pp.ESE-4.
- 600 Aochi, H. and Olsen, K., 2004. On the effects of non-planar geometry for blind thrust faults on  
601 strong ground motion. In *Computational Earthquake Science Part II* (pp. 2139-2153).  
602 Birkhäuser, Basel.
- 603 Aydin, A. and Du, Y., 1995. Surface rupture at a fault bend: The 28 June 1992 Landers,  
604 California, earthquake. *Bulletin of the Seismological Society of America*, 85(1), pp.111-128.
- 605 Becker, T.W., Hardebeck, J.L. and Anderson, G., 2005. Constraints on fault slip rates of the  
606 southern California plate boundary from GPS velocity and stress inversions. *Geophysical  
607 Journal International*, 160(2), pp.634-650.
- 608 Bemis, S., Scharer, K.M., Dolan, J.F. and Rhodes, E., 2016. The Elizabeth Lake paleoseismic  
609 site: Rupture pattern constraints for the past~ 800 years for the Mojave section of the south-  
610 central San Andreas Fault. In *7th international INQUA workshop on paleoseismology, active  
611 tectonics and archaeoseismology*.
- 612 Beyer, J., Cooke, M.L. and Marshall, S.T., 2018. Sensitivity of deformation to activity along the  
613 Mill Creek and Mission Creek strands of the southern San Andreas fault. *Geosphere*, 14(6),  
614 pp.2296-2310.
- 615 Biasi, G.P., Weldon, R.J., Fumal, T.E. and Seitz, G.G., 2002. Paleoseismic event dating and the  
616 conditional probability of large earthquakes on the southern San Andreas fault,  
617 California. *Bulletin of the Seismological Society of America*, 92(7), pp.2761-2781.
- 618 Biasi, G.P. and Weldon, R.J., 2009. San Andreas fault rupture scenarios from multiple  
619 paleoseismic records: Stringing pearls. *Bulletin of the Seismological Society of America*,  
620 99,2A, pp. 471-498.
- 621 Bryant, W.A., 1992. Surface rupture along the Johnson Valley, Homestead Valley, and related  
622 faults associated with the M 7.5 28 June 1992 Landers Earthquake. *Div. Mines Geol. Fault  
623 Eval. Rep*, 234.
- 624 Bryant, W.A., 1994. Surface fault rupture along the Homestead Valley, Emerson, and related  
625 faults associated with the Mw 7.3 28 June 1992 Landers earthquake. *Fault Eval. Rep*.



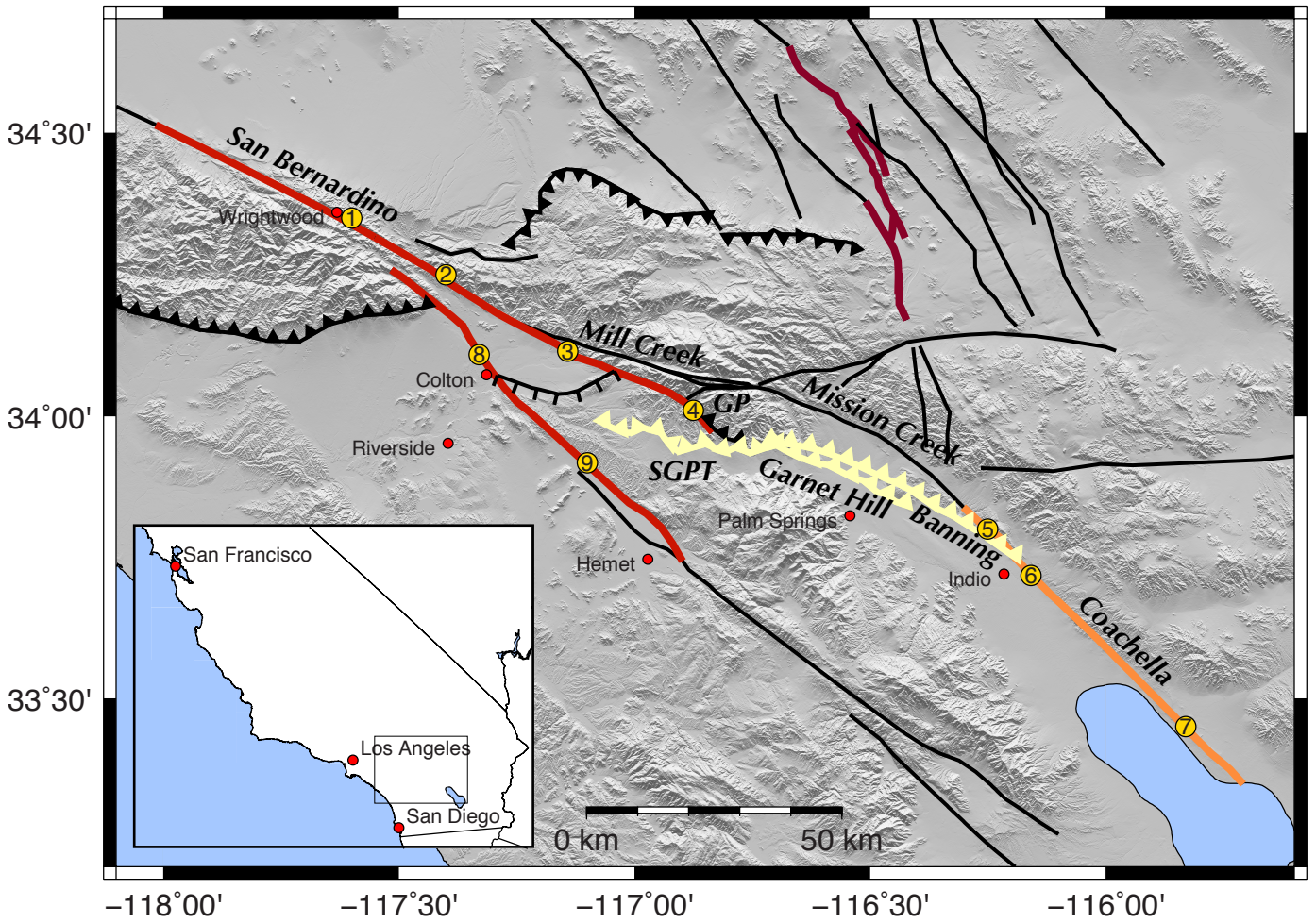
- 626        *FER*, 239, p.18.
- 627        Carpenter, B.M., Saffer, D.M. and Marone, C., 2012. Frictional properties and sliding stability of  
628        the San Andreas fault from deep drill core. *Geology*, 40(8), pp.759-762.
- 629        Cooke, M.L. and Dair, L.C., 2011. Simulating the recent evolution of the southern big bend of  
630        the San Andreas fault, southern California. *Journal of Geophysical Research: Solid*  
631        *Earth*, 116(B4).
- 632        Crider, J.G. and Pollard, D.D., 1998. Fault linkage: Three-dimensional mechanical interaction  
633        between echelon normal faults. *Journal of Geophysical Research: Solid Earth*, 103(B10),  
634        pp.24373-24391.
- 635        Dawers, N.H. and Anders, M.H., 1995. Displacement-length scaling and fault linkage. *Journal of*  
636        *Structural Geology*, 17(5), pp.607-614.
- 637        DeMets, C. and Dixon, T.H., 1999. New kinematic models for Pacific-North America motion  
638        from 3 Ma to present, I: Evidence for steady motion and biases in the NUVEL-1A  
639        model. *Geophysical Research Letters*, 26(13), pp.1921-1924.
- 640        Di Toro, G., Hirose, T., Nielsen, S. and Shimamoto, T., 2006. Relating high-velocity rock-  
641        friction experiments to coseismic slip in the presence of melts. *Geophysical Monograph-*  
642        *American Geophysical Union*, 170, p.121.
- 643        Douilly, R., Oglesby, D.D., Cooke, M.L. and Beyer, J.L., 2017, December. Dynamic Models of  
644        Earthquake Rupture along branch faults of the Eastern San Gorgonio Pass Region in CA  
645        using Complex Fault Structure. In *AGU Fall Meeting Abstracts*.
- 646        Duan, B. and Oglesby, D.D., 2005. Multicycle dynamics of nonplanar strike-slip faults. *Journal*  
647        *of Geophysical Research: Solid Earth*, 110(B3).
- 648        Duan, B. and Oglesby, D.D., 2006. Heterogeneous fault stresses from previous earthquakes and  
649        the effect on dynamics of parallel strike-slip faults. *Journal of Geophysical Research: Solid*  
650        *Earth*, 111(B5).
- 651        Duan, B. and Oglesby, D.D., 2007. Nonuniform prestress from prior earthquakes and the effect  
652        on dynamics of branched fault systems. *Journal of Geophysical Research: Solid*  
653        *Earth*, 112(B5).
- 654        Fattaruso, L.A., Cooke, M.L. and Dorsey, R.J., 2014. Sensitivity of uplift patterns to dip of the  
655        San Andreas fault in the Coachella Valley, California. *Geosphere*, 10(6), pp.1235-1246.
- 656        Fay, N.P. and Humphreys, E.D., 2005. Fault slip rates, effects of elastic heterogeneity on  
657        geodetic data, and the strength of the lower crust in the Salton Trough region, southern  
658        California. *Journal of Geophysical Research: Solid Earth*, 110(B9).
- 659        Field, E.H., Arrowsmith, R.J., Biasi, G.P., Bird, P., Dawson, T.E., Felzer, K.R., Jackson, D.D.,  
660        Johnson, K.M., Jordan, T.H., Madden, C. and Michael, A.J., 2014. Uniform California  
661        earthquake rupture forecast, version 3 (UCERF3)—The time-independent model. *Bulletin of*  
662        *the Seismological Society of America*, 104(3), pp.1122-1180.
- 663        Fosdick, J.C. and Bisniuk, K., 2018. Sedimentary signals of recent faulting along an old strand of  
664        the San Andreas Fault, USA. *Scientific reports*, 8(1), p.12132.
- 665        Fulton, P.M., Brodsky, E.E., Kano, Y., Mori, J., Chester, F., Ishikawa, T., Harris, R.N., Lin, W.,  
666        Eguchi, N. and Toczko, S., 2013. Low coseismic friction on the Tohoku-Oki fault determined  
667        from temperature measurements. *Science*, 342(6163), pp.1214-1217.
- 668        Fumal, T.E., Rymer, M.J. and Seitz, G.G., 2002. Timing of large earthquakes since AD 800 on  
669        the Mission Creek strand of the San Andreas fault zone at Thousand Palms Oasis, near Palm  
670        Springs, California. *Bulletin of the Seismological Society of America*, 92(7), pp.2841-2860.
- 671        Goebel, T.H.W., Hauksson, E., Shearer, P.M. and Ampuero, J.P., 2015. Stress-drop

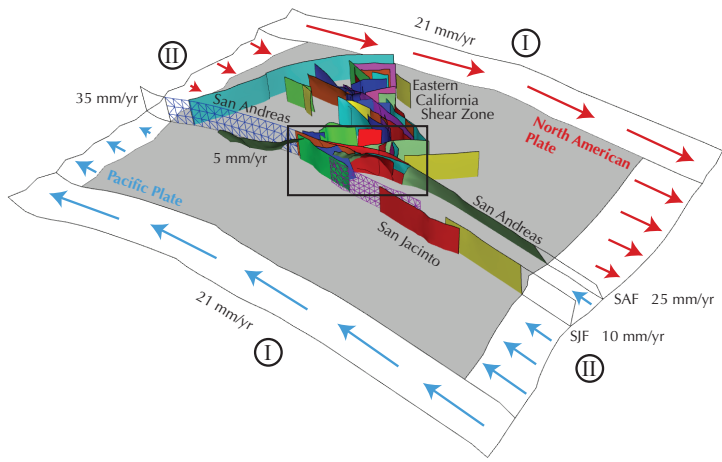
- 672 heterogeneity within tectonically complex regions: a case study of San Gorgonio Pass,  
673 southern California. *Geophysical Journal International*, 202(1), pp.514-528.
- 674 Goldsby, D.L. and Tullis, T.E., 2011. Flash heating leads to low frictional strength of crustal  
675 rocks at earthquake slip rates. *Science*, 334(6053), pp.216-218.
- 676 Hardebeck, J.L. and Hauksson, E., 2001. Crustal stress field in southern California and its  
677 implications for fault mechanics. *Journal of Geophysical Research: Solid Earth*, 106(B10),  
678 pp.21859-21882.
- 679 Hart, E.W., Bryant, W.A., and J.A. Treiman, 1993. Surface faulting associated with the June  
680 1992 Landers earthquake, California. *Calif. Geol.* 46, pp.10-16.
- 681 Heermance, R.V. and Yule, D., 2017. Holocene slip rates along the San Andreas Fault System in  
682 the San Gorgonio Pass and implications for large earthquakes in southern  
683 California. *Geophysical Research Letters*, 44(11), pp.5391-5400.
- 684 Herbert, J.W. and Cooke, M.L., 2012. Sensitivity of the southern San Andreas fault system to  
685 tectonic boundary conditions and fault configurations. *Bulletin of the Seismological Society of  
686 America*, 102(5), pp.2046-2062.
- 687 Herbert, J.W., Cooke, M.L. and Marshall, S.T., 2014a. Influence of fault connectivity on slip  
688 rates in southern California: Potential impact on discrepancies between geodetic derived and  
689 geologic slip rates. *Journal of Geophysical Research: Solid Earth*, 119(3), pp.2342-2361.
- 690 Kame, N., Rice, J.R. and Dmowska, R., 2003. Effects of prestress state and rupture velocity on  
691 dynamic fault branching. *Journal of Geophysical Research: Solid Earth*, 108(B5).
- 692 Kase, Y. and Day, S.M., 2006. Spontaneous rupture processes on a bending fault. *Geophysical  
693 Research Letters*, 33(10).
- 694 Kendrick, K.J. and Fumal, T.E., 2005, October. Paleoseismicity of the northern San Jacinto fault,  
695 Colton and San Bernardino, southern California; preliminary results. In *2005 Salt Lake City  
696 Annual Meeting*.
- 697 Kendrick, K.J., Matti, J.C. and Mahan, S.A., 2015. Late Quaternary slip history of the Mill Creek  
698 strand of the San Andreas fault in San Gorgonio Pass, southern California: The role of a  
699 subsidiary left-lateral fault in strand switching. *Bulletin*, 127(5-6), pp.825-849.
- 700 King, G.C., Stein, R.S. and Lin, J., 1994. Static stress changes and the triggering of  
701 earthquakes. *Bulletin of the Seismological Society of America*, 84(3), pp.935-953.
- 702 Li, H., Xue, L., Brodsky, E.E., Mori, J.J., Fulton, P.M., Wang, H., Kano, Y., Yun, K., Harris,  
703 R.N., Gong, Z. and Li, C., 2015. Long-term temperature records following the Mw 7.9  
704 Wenchuan (China) earthquake are consistent with low friction. *Geology*, 43(2), pp.163-166.
- 705 Loveless, J.P. and Meade, B.J., 2011. Stress modulation on the San Andreas fault by interseismic  
706 fault system interactions. *Geology*, 39(11), pp.1035-1038.
- 707 Lozos, J.C., Oglesby, D.D., Brune, J.N. and Olsen, K.B., 2012. Small intermediate fault  
708 segments can either aid or hinder rupture propagation at stepovers. *Geophysical Research  
709 Letters*, 39(18).
- 710 Lozos, J.C., 2016. A case for historic joint rupture of the San Andreas and San Jacinto  
711 faults. *Science advances*, 2(3), p.e1500621.
- 712 Madden, E.H. and Pollard, D.D., 2012. Integration of surface slip and aftershocks to constrain  
713 the 3D structure of faults involved in the M 7.3 Landers earthquake, Southern  
714 California. *Bulletin of the Seismological Society of America*, 102(1), pp.321-342.
- 715 Maerten, L., Willemsse, E.J., Pollard, D.D. and Rawnsley, K., 1999. Slip distributions on  
716 intersecting normal faults. *Journal of Structural Geology*, 21(3), pp.259-272.
- 717 Marshall, S.T., Cooke, M.L. and Owen, S.E., 2009. Interseismic deformation associated with

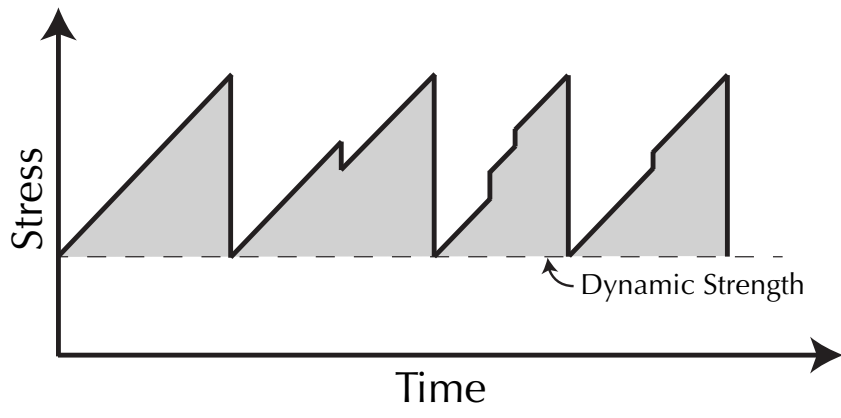
- 718 three-dimensional faults in the greater Los Angeles region, California. *Journal of Geophysical*  
719 *Research: Solid Earth*, 114(B12).
- 720 Matti, J.C., Morton, D.M. and Cox, B.F., 1992. *The San Andreas fault system in the vicinity of*  
721 *the central Transverse Ranges province, southern California* (No. 92-354). US Geological  
722 Survey,.
- 723 McGill, S., Dergham, S., Barton, K., Berney-Ficklin, T., Grant, D., Hartling, C., Hobart, K.,  
724 Minnich, R., Rodriguez, M., Runnerstrom, E. and Russell, J., 2002. Paleoseismology of the  
725 San Andreas fault at Plunge Creek, near San Bernardino, southern California. *Bulletin of the*  
726 *Seismological Society of America*, 92(7), pp.2803-2840.
- 727 McPhillips, D. and Scharer, K.M., 2018. Quantifying uncertainty in cumulative surface slip  
728 along the Cucamonga Fault, a crustal thrust fault in southern California. *Journal of*  
729 *Geophysical Research: Solid Earth*, 123(10), pp.9063-9083.
- 730 Meade, B.J. and Hager, B.H., 2005. Block models of crustal motion in southern California  
731 constrained by GPS measurements. *Journal of Geophysical Research: Solid Earth*, 110(B3).
- 732 Nicholson, C., Plesch, A., and Shaw, J.H., 2017. Community Fault Model Version 5.2: Updating  
733 and expanding the CFM 3D fault set and its associated fault database: Poster Presentation at  
734 2017 Southern California Earthquake Center (SCEC) Annual Meeting.
- 735 Oglesby, D.D., Day, S.M. and O'Connell, D.R., 2003. Dynamic and static interaction of two  
736 thrust faults: A case study with general implications. *Journal of Geophysical Research: Solid*  
737 *Earth*, 108(B10).
- 738 Oglesby, D.D., 2005. The dynamics of strike-slip step-overs with linking dip-slip faults. *Bulletin*  
739 *of the Seismological Society of America*, 95(5), pp.1604-1622.
- 740 Onderdonk, N.W., Rockwell, T.K., McGill, S.F. and Marliyani, G.I., 2013. Evidence for seven  
741 surface ruptures in the past 1600 years on the Claremont fault at Mystic Lake, northern San  
742 Jacinto fault zone, California. *Bulletin of the Seismological Society of America*, 103(1),  
743 pp.519-541.
- 744 Onderdonk, N.W., McGill, S.F. and Rockwell, T.K., 2015. Short-term variations in slip rate and  
745 size of prehistoric earthquakes during the past 2000 years on the northern San Jacinto fault  
746 zone, a major plate-boundary structure in southern California. *Lithosphere*, 7(3), pp.211-234.
- 747 Onderdonk, N., McGill, S. and Rockwell, T., 2018. A 3700 yr paleoseismic record from the  
748 northern San Jacinto fault and implications for joint rupture of the San Jacinto and San  
749 Andreas faults. *Geosphere*, 14(6), pp.2447-2468.
- 750 Philibosian, B., Fumal, T. and Weldon, R., 2011. San Andreas fault earthquake chronology and  
751 Lake Cahuilla history at Coachella, California. *Bulletin of the Seismological Society of*  
752 *America*, 101(1), pp.13-38.
- 753 Plesch, A., Shaw, J.H., Benson, C., Bryant, W.A., Carena, S., Cooke, M., Dolan, J., Fuis, G.,  
754 Gath, E., Grant, L. and Hauksson, E., 2007. Community fault model (CFM) for southern  
755 California. *Bulletin of the Seismological Society of America*, 97(6), pp.1793-1802.
- 756 Pollitz, F.F. and Sacks, I.S., 2002. Stress triggering of the 1999 Hector Mine earthquake by  
757 transient deformation following the 1992 Landers earthquake. *Bulletin of the Seismological*  
758 *Society of America*, 92(4), pp.1487-1496.
- 759 Richards-Dinger, K. and Dieterich, J.H., 2012. RSQSim earthquake simulator. *Seismological*  
760 *Research Letters*, 83(6), pp.983-990.
- 761 Rockwell, T.K., Dawson, T.E., Ben-Horin, J.Y. and Seitz, G., 2015. A 21-event, 4,000-year  
762 history of surface ruptures in the Anza seismic gap, San Jacinto Fault, and implications for  
763 long-term earthquake production on a major plate boundary fault. *Pure and Applied*

- 764        *Geophysics*, 172(5), pp.1143-1165.
- 765 Rockwell, T.K., Meltzner, A.J. and Haaker, E.C., 2018. Dates of the Two Most Recent Surface  
766 Ruptures on the Southernmost San Andreas Fault Recalculated by Precise Dating of Lake  
767 Cahuilla Dry Periods. *Bulletin of the Seismological Society of America*, 108(5A), pp.2634-  
768 2649.
- 769 Seitz, G., Weldon II, R. and Biasi, G.P., 1997. The Pitman Canyon paleoseismic record: A re-  
770 evaluation of southern San Andreas fault segmentation. *Journal of Geodynamics*, 24(1-4),  
771 pp.129-138.
- 772 Sharp, R.V., 1981. Variable rates of late Quaternary strike slip on the San Jacinto fault zone,  
773 southern California. *Journal of Geophysical Research: Solid Earth*, 86(B3), pp.1754-1762.
- 774 Sieh, K.E., 1986. Slip rate across the San Andreas fault and prehistoric earthquakes at Indio,  
775 California. *Eos Trans. AGU*, 67(44), p.1200.
- 776 Sieh, K.E. and Williams, P.L., 1990. Behavior of the southernmost San Andreas fault during the  
777 past 300 years. *Journal of Geophysical Research: Solid Earth*, 95(B5), pp.6629-6645.
- 778 Sieh, K., Jones, L., Hauksson, E., Hudnut, K., Eberhart-Phillips, D., Heaton, T., Hough, S.,  
779 Hutton, K., Kanamori, H., Lilje, A. and Lindvall, S., 1993. Near-field investigations of the  
780 Landers earthquake sequence, April to July 1992. *Science*, 260(5105), pp.171-176.
- 781 Simpson, R.W., 1997. Quantifying Anderson's fault types. *Journal of Geophysical Research:*  
782 *Solid Earth*, 102(B8), pp.17909-17919.
- 783 Smith, B.R. and Sandwell, D.T., 2006. A model of the earthquake cycle along the San Andreas  
784 Fault System for the past 1000 years. *Journal of Geophysical Research: Solid Earth*, 111(B1).
- 785 Smith-Konter, B. and Sandwell, D., 2009. Stress evolution of the San Andreas fault system:  
786 Recurrence interval versus locking depth. *Geophysical Research Letters*, 36(13).
- 787 Stein, R.S., 1999. The role of stress transfer in earthquake occurrence. *Nature*, 402(6762), p.605.
- 788 Tarnowski, J.M., 2017. *The Effects of Dynamic Stress on Fault Interaction and Earthquake*  
789 *Triggering in the San Gorgonio Pass and San Jacinto, CA Regions*. University of California,  
790 Riverside.
- 791 Thomas, A.L., 1993. *Poly 3 D: a three-dimensional, polygonal element, displacement*  
792 *discontinuity boundary element computer program with applications to fractures, faults, and*  
793 *cavities in the Earth's crust* (Master's thesis, to the Department of Geology, Stanford  
794 University).
- 795 Tong, X., Smith-Konter, B. and Sandwell, D.T., 2014. Is there a discrepancy between geological  
796 and geodetic slip rates along the San Andreas Fault System?. *Journal of Geophysical*  
797 *Research: Solid Earth*, 119(3), pp.2518-2538.
- 798 Weldon, R.J. and Sieh, K.E., 1985. Holocene rate of slip and tentative recurrence interval for  
799 large earthquakes on the San Andreas fault, Cajon Pass, southern California. *Geological*  
800 *Society of America Bulletin*, 96(6), pp.793-812.
- 801 Weldon, R.J., Fumal, T.E., Powers, T.J., Pezzopane, S.K., Scharer, K.M. and Hamilton, J.C.,  
802 2002. Structure and earthquake offsets on the San Andreas fault at the Wrightwood,  
803 California, paleoseismic site. *Bulletin of the Seismological Society of America*, 92(7),  
804 pp.2704-2725.
- 805 Willemse, E.J. and Pollard, D.D., 1998. On the orientation and patterns of wing cracks and  
806 solution surfaces at the tips of a sliding flaw or fault. *Journal of Geophysical Research: Solid*  
807 *Earth*, 103(B2), pp.2427-2438.
- 808 Yule, D. and Howland, C., 2001. A revised chronology of earthquakes produced by the San  
809 Andreas fault at Burro Flats, near Banning, California. In *SCEC Annual Meeting, Proceedings*

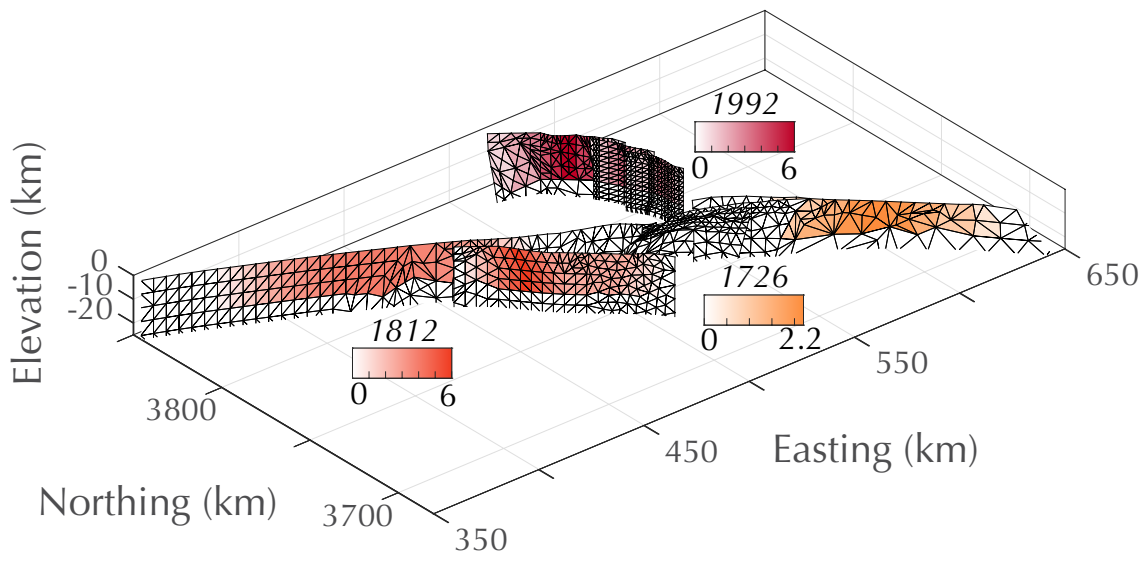
- 810        *and Abstracts.*
- 811        Yule, D. and Sieh, K., 2003. Complexities of the San Andreas fault near San Gorgonio Pass:  
812        Implications for large earthquakes. *Journal of Geophysical Research: Solid Earth*, 108(B11).
- 813        Yule, D., Scharer, K., Sieh, K., Wolff, L., McBurnett, P., Ramzan, S., Witkosky, R. and  
814        Desjarlais, I., 2014. Paleoseismology and slip rate of the San Andreas fault system at San  
815        Gorgonio Pass.

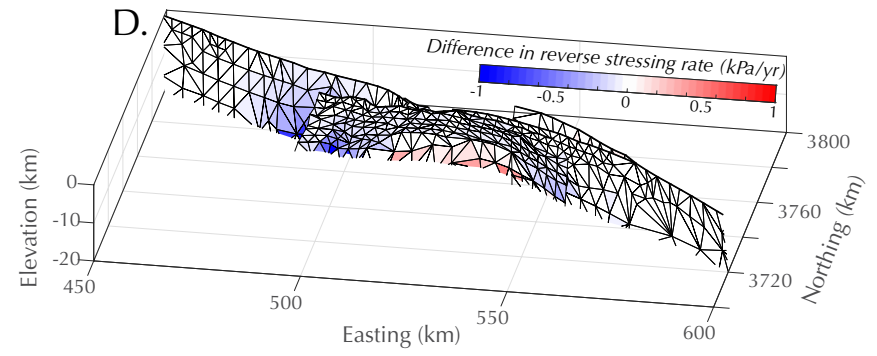
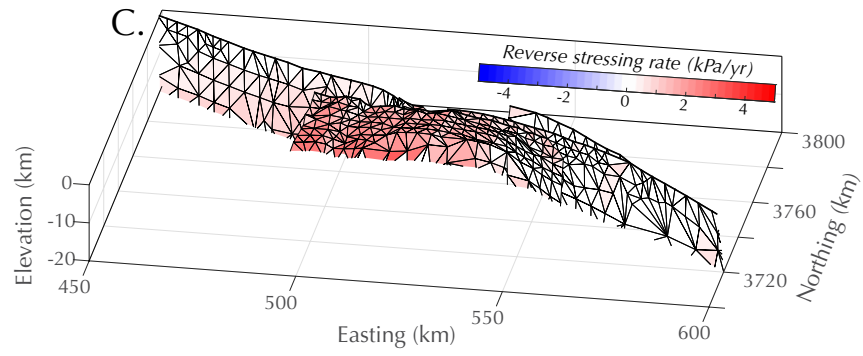
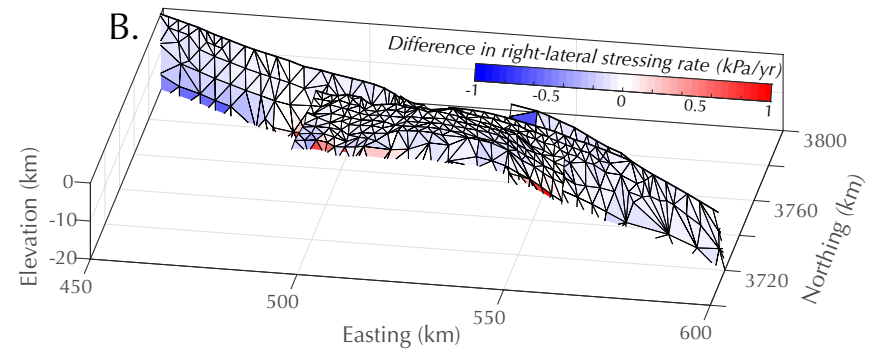
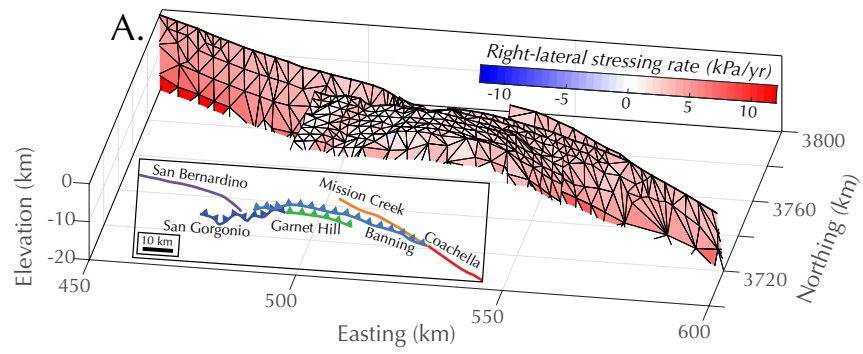


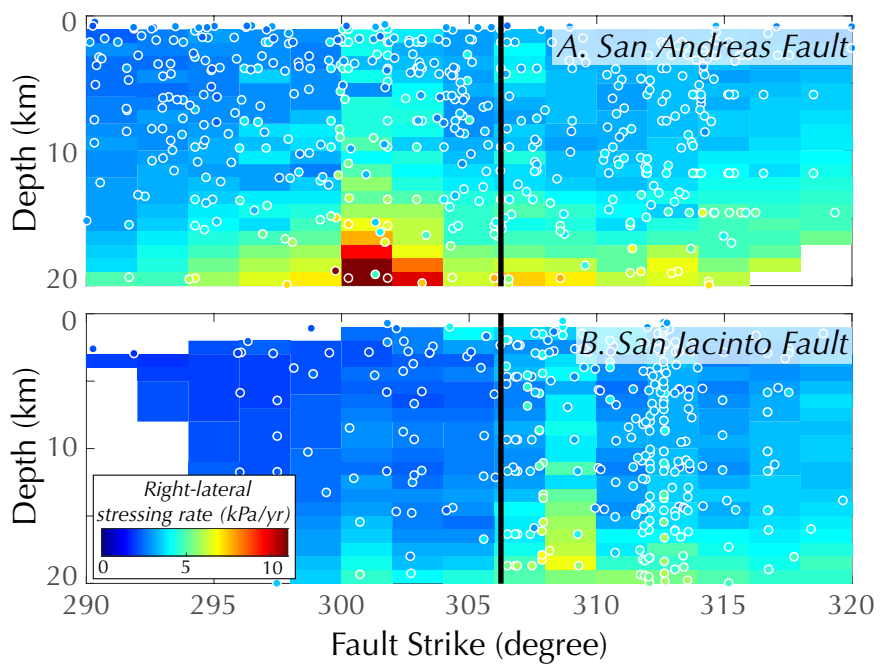


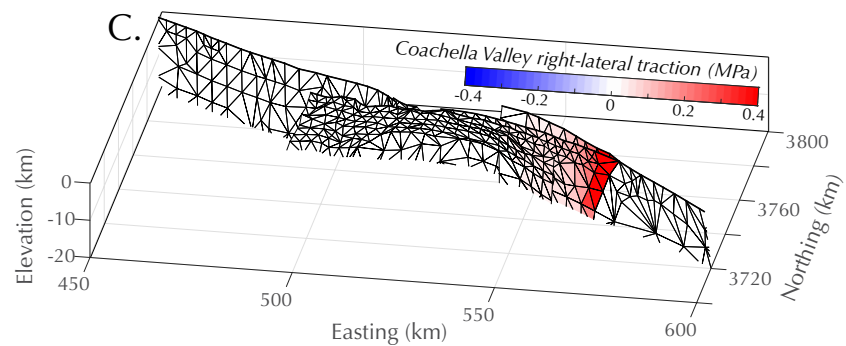
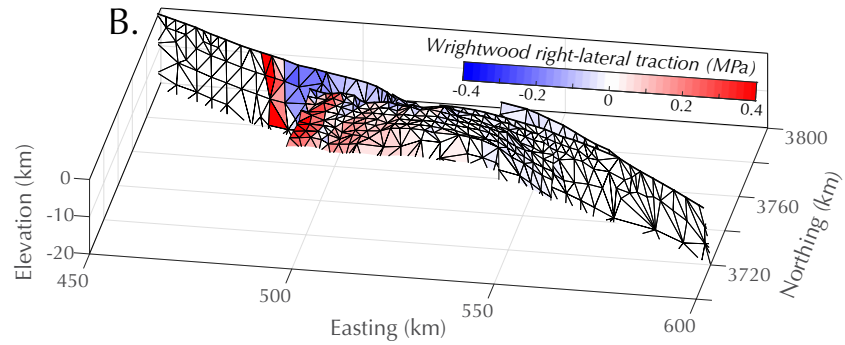
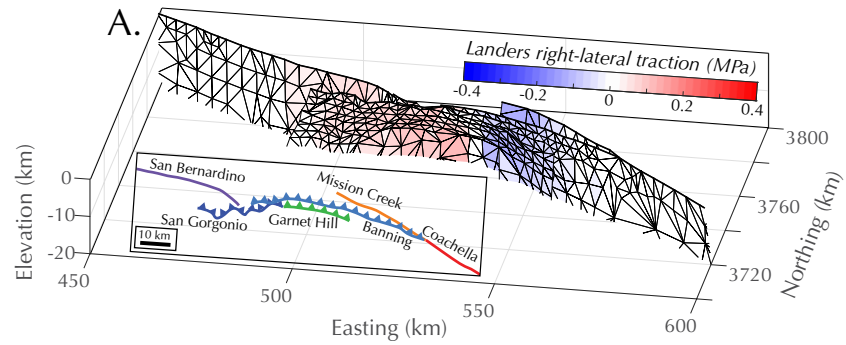


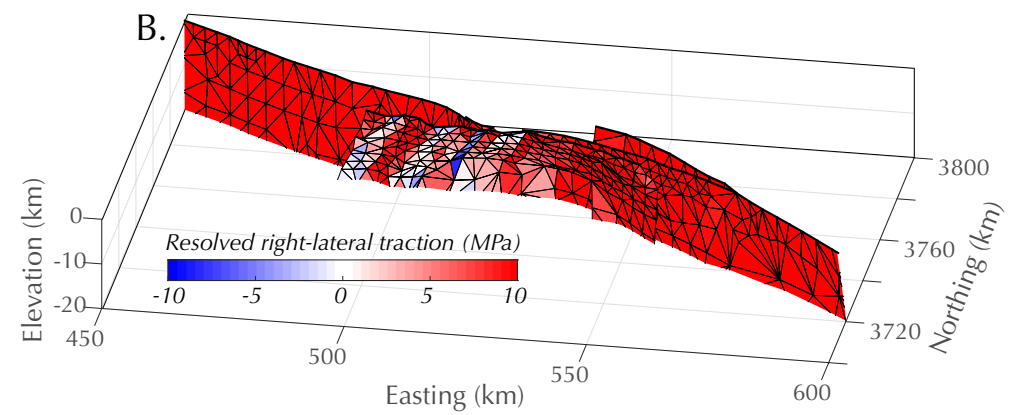
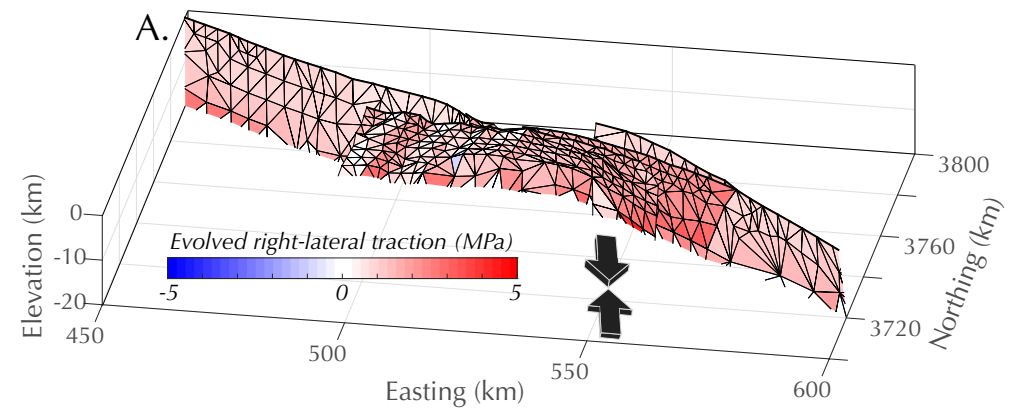


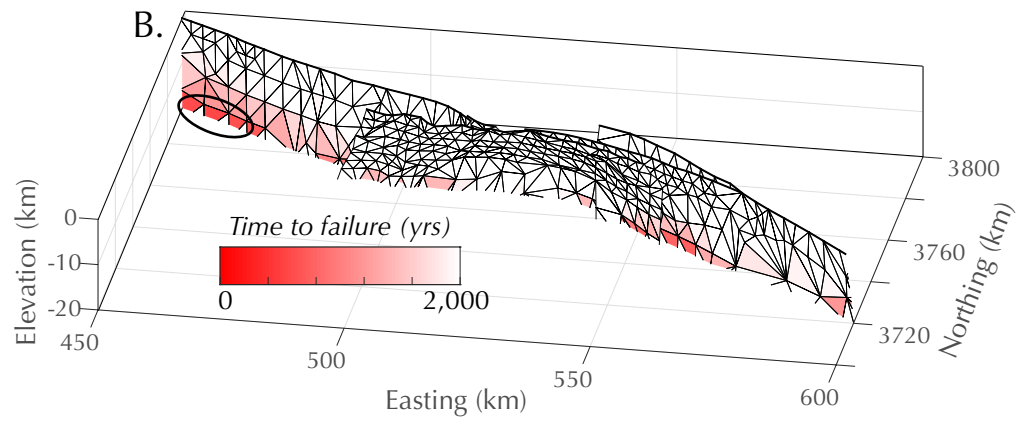
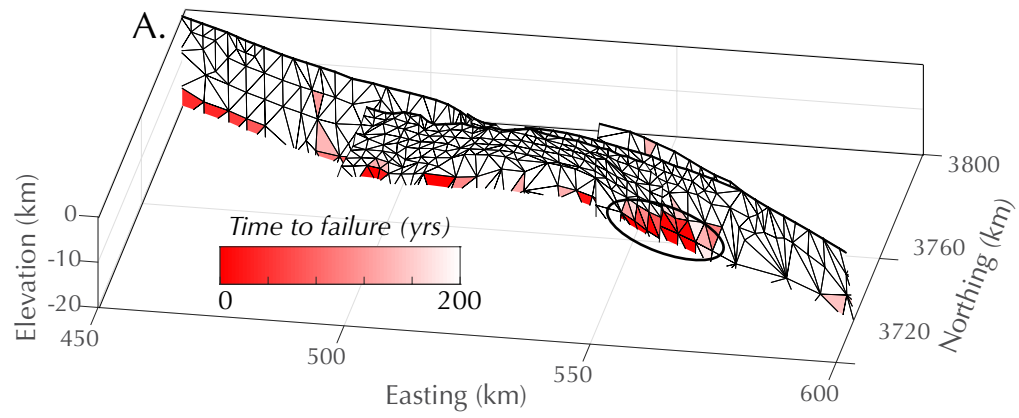












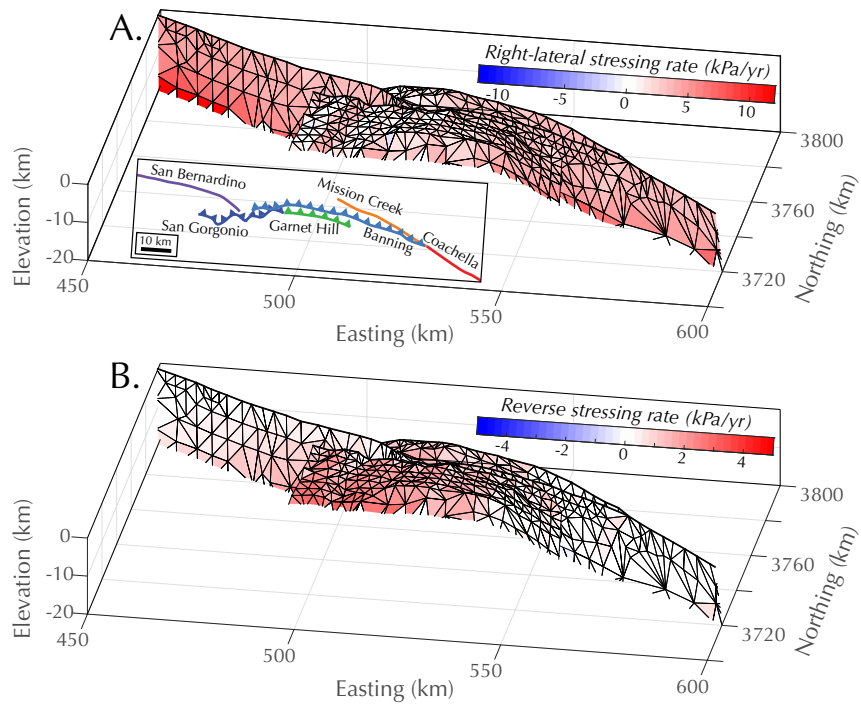


Figure S1. Right-lateral (A) and reverse dip slip (B) stressing rates for the alternative fault configuration from Beyer et al. (2018).